Supporting Information

Supporting Experimental

Materials and methods

Metal nitrate stock solutions were prepared from iron(III) nitrate nonahydrate and magnesium nitrate hexahydrate (1 g of solid dissolved in 10 ml with deionized water). Gelatin solution was prepared by dissolving 10 g gelatin (G2500, Sigma Aldrich) in 90 g hot deionized water. Iron and magnesium nitrate solutions were premixed and added with vigorous stirring to hot gelatin solution (20 g) to give a total of 0.01 moles of metal salts. Exact volumes are detailed in Table S1. The mixture crosslinks strongly and has to be heated to ensure complete mixing and formation of a viscous liquid. Samples were dried in open beakers at 80 °C in air and heated at 10 °C/min to 800 °C with 5 min dwell in covered crucibles under a steady nitrogen flow. The samples were cooled to <40 °C inside the furnace under N_2 flow. Samples were washed by adding 0.1 g of powder to 20 ml HCl (0.1 M), sonicating in a bath for 1 hour and then stirring for 23 hours. The powders were collected by centrifugation, washed with deionized water (*3) and ethanol (*1) and dried at room temperature.
Exact volumes of the stock solutions to generate the samples and controls are detailed in Table S1.

Sample code	Molar ratio Fe:Mg	Volume $Fe(NO_3)_3$ (ml)	Volume $Mg(NO_3)_2$ (ml)
MF0	0:100	0.00	25.60
MF25	25:75	10.10	19.20
MF50	50:50	20.20	12.80
MF100	100:0	40.40	0.00

Table S1 Volumes of stock solutions mixed with 20 g of 10% (by mass) gelatin solution.

NB: Samples were also prepared using different biopolymer:metal ratio (10g and 30g of gelatin solution for the same volumes of metal solutions). Synchrotron XRD showed that the MgO/Fe_3C composite was still formed. Furthermore, the synthesis was successfully repeated in both tube and muffle furnaces and at a larger scale in a 1L capacity crucible, indicating the robustness of the method.

Characterization techniques

NB: Samples were ground to fine powders for all characterization, in order to ensure homogeneity.

SXRD: The complex mixture of nanoparticles resulted in very broad and overlapping XRD peaks. The samples were therefore analysed using the Spring-8 BL15XU synchrotron beamline (λ = 0.65297 Å) equipped with imaging plate[1] to maximize peak resolution and signal to noise ratio. Additionally, the low divergence X-ray beam from the synchrotron radiation light source reduces the effect of line broadening. Samples were ground to fine powders and loaded into Lindemann Glass capillary tubes for analysis.

Electron Microscopy: SEM images were recorded using a JEOL JSM-7001F field emission scanning electron microscope equipped with SEI and COMPO detectors. Samples were prepared by depositing on conductive carbon substrates and coating with Pt/Pd. High resolution images were recorded from uncoated samples. TEM images were recorded using a JEOL JEM-2100F transmission electron microscope equipped with CCD camera, STEM dark field detector, and Scanning Energy Dispersive X-ray Analysis. Samples were prepared by dispersing in ethanol and dropping onto holey carbon-coated copper grids.

Thermogravimetric Analysis: TGA measurements were performed on SII Exstar 6000 (TG-DTA 6200) under N_2 (50 mL/min, 10 °C/min). Sample mass was typically 30 mg.

Nitrogen porosimetry: The Brunauer-Emmett-Teller (BET) surface area was obtained by nitrogen sorption experiments using a BELSORP Mini (BEL Japan) Gas Sorption System at 77 K. Samples were dried initially at room temperature under vacuum for 1 hour to avoid surface oxidation by adsorbed water then gradually heated to 80 °C and left overnight. BET surface areas were calculated using a linear section of points for $0.02 < p/p_0 < 0.3$.

Elemental Analysis: Metal content was measured using ICP (Inductively Coupled Plasma) Mass Spectrometry. Samples (4-5 mg) were fused with a mixture of Na_2CO_3 (0.5 g) and H_3BO_3 (0.2 g) in a platinum crucible at 1000 °C for 7 minutes. The melt was dissolved in HCl (2 ml) and dilutions prepared for analysis. Analysis machine: Nippon Jarrell-Ash Co., Model: IRIS Advantage. Other elemental analysis was undertaken by Carbon/Sulfur Determiner (LECO Co., CS-444LS) equipped with induction furnace, infrared absorption detector, using $CaCO_3$ as the standard sample. Also, an

Oxygen/Nitrogen Determiner (LECO Co., TC-436AR) equipped with an impulse furnace and thermal conductivity detector, using Si_3N_4 as the standard sample.

Small Angle X-ray Scattering: SAXS measurements were performed on a pinhole-collimated, PILATUS detector-equipped instrument, built around a rotating anode source using a molybdenum target ($\lambda = 0.07093$ nm). Measurements were recorded using two sample-to-detector distances for a wide q-range coverage (<0.2 to >10.0 nm^{-1}). Measurements were corrected for natural background radiation, transmission, sample thickness, measurement time, primary beam flux, parasitic background, polarization, detector solid angle coverage, and sample-self-absorption using in-house developed data-reduction software. Deadtime corrections are considered unnecessary at the observed count-rates, and flatfield corrections are performed by the detector image acquisition software prior to ingestion by the data reduction software. With these corrections, the minimum relative uncertainty of the data is estimated at around 1%, and the absolute uncertainty is estimated to be around 10%.[2] The data is scaled to absolute units using a calibrated glassy carbon sample.[3] Intensity uncertainties have been propagated throughout the procedure as described, and are used as weights in the fitting procedure.

The fitting procedure consists of a Monte-Carlo-based method assuming spherical subunits.[4] All scattering patterns can be described on average to within 2 standard deviations of the intensity. The size information obtained is related to the q-range fitted, which was 0.2-10 nm^{-1}, corresponding to minimum and maximum distinguishable structural radii of 0.3-15 nm. The size histograms resulting from the MC procedure have been plotted as volume-weighted size distributions.

As both the volume fraction and the electron density contrast of the scattering phases are ill-defined, the height of each bar assumes the relative scattering power, *RSP*. This is proportional to the volume fraction of the material and its contrast squared ($\Delta\rho^2$) i.e. $RSP = [\phi\Delta\rho^2]_{rel}$, and thus independent from either unknown. *RSP* is normalised to the maximum integrated scattering power for a single sample (MF50), to enable comparison between samples. The absolute values have therefore no meaning, but can be compared from sample to sample. The contrast derives from the difference in electron densities, ρ, of each material versus carbon, *i.e.* $\Delta\rho$, with relative values of 17, 13 and 45 for air, MgO and Fe_3C respectively, assuming that the bulk consists of mainly amorphous carbon. Therefore, the relative contribution from the pores and MgO, Fe_3C nanoparticles to scattering power from contrast, *i.e.* $\Delta\rho^2$, should scale as 1.0 : 0.6 : 7.0. For example, this explains the increase in scattering power by a factor of 1.5-2 throughout region R2 that occurs upon the replacement of MgO with air after etching.

The alternative approach to that outlined above would scale each region R1-3 by the contrast of the dominant component as stipulated in the MS. However, in this case the contributions from other components to scattering within each region would be ignored. It is felt in this case that the more general solution applied here is preferable and future experiments, combining SAXS with small-angle neutron scattering (SANS) or ultra-small angle techniques[5,6] are expected to further elucidate the detailed structure of this system.

Electrochemical experiments: The evaluation of ORR activity of various electrocatalysts (MF0-E, MF25-E, MF50-E, MF25-Ec and commercial Pt/C, HiSPECTM 3000, 20% Pt on carbon black, Johnson Matthey) was performed in standard three-electrode glass cell on a CHI 660D workstation (USA). A rotating disk glassy carbon electrode (RRDE-3A, ALS, Japan) modified with the electrocatalyst was used as the working electrode. A Pt wire and Ag/AgCl (saturated KCl) were used as a counter and reference electrodes, respectively. The electrolyte (0.1 M KOH in water) was freshly prepared. The procedure of the working electrode modification is as follows. Firstly, the rotating glassy carbon electrode was carefully polished to obtain a mirror-like surface with an Electrode Polishing kit (ALS, Japan). Then, 20 μL of the electrocatalyst suspension in ethanol (1 mg/mL) was cast on the surface of rotating glassy carbon electrode. The electrode was allowed to dry at room temperature and further heated in air at 60 ^{o}C for 15 min. After that, 5 μL of Nafion (0.05 wt.%) was further cast on the surface of the electrode. Lastly, the electrode was again dried at room temperature and heated in air at 60 ^{o}C for 15 min. For a fair comparison, the same amount of each catalyst by mass was loaded on a glassy carbon rotating-disk electrode.

The Koutecky-Levich equations, used for calculating the number of electrons involved in each catalytic reduction process, are listed as follows:

$$\frac{1}{J} = \frac{1}{J_L} + \frac{1}{J_K} = \frac{1}{B\omega^{1/2}} + \frac{1}{J_K} \qquad \text{Equation 1}$$

$$B = 0.62nFC_0(D_0)^{2/3}\nu^{-1/6} \qquad \text{Equation 2}$$

$$J_K = nFkC_0$$

Equation 3

in which *J* is the measured current density, J_K and J_L are the kinetic- and diffusion-limiting current densities, ω is the angular velocity of the rotating electrode (ω =2πN, N is the linear rotation speed), n is the exchange electron transfer number in ORR, *F* is the Faraday constant (F=96485 C/mol), C_0 is the concentration of O_2, D_0 is the diffusion coefficient of O_2, *v* is the kinematic viscosity of the electrolyte, and *k* is the electron transfer rate constant., Since the electrolyte was O_2 saturated 0.1 M KOH in this report, C_0, D_0 *and v* was used as 1.2×10^{-3} M, 1.9×10^{-5} cm^2/s, and 0.01 cm^2/s, respectively.

Supporting Discussion

On effect of Mg/Fe on cross-linking density

Figures S3a S3b and S3c show a series of samples prepared with constant [$Fe(NO_3)_3$] and [gelatin] but increasing [$Mg(NO_3)_2$]. $Mg(NO_3)_2$ alone does not appear to cross-link the gelatin, simply forming a homogeneous solution when mixed. From the texture of the gels (Figure S3a), it is clear that the presence of Mg induced much stronger binding of Fe(III) to the gelatin polymer. The samples became considerably more 'rubbery' with increasing [Mg(II)]. This suggests that Mg(II) enhances the binding of Fe(III) to the polymer. Gelatin has many different functional groups, so there are several possible cation binding sites. The presence of Mg(II) may change the solution conformation of the polymer, facilitating more Fe(III) crosslinking.

On the mechanistic investigation

To identify the formation mechanism of the nanocomposites, samples were quenched at 600 °C and 700 °C and characterized by sXRD (Figures S7-8). Broad, low intensity peaks at 600 °C indicate very small crystallites of MgO, while broad peaks for Fe_3C emerge at 700 °C. Previously, it was found that the synthesis of Fe_3C from gelatin[7] proceeded via magnetite (Fe_3O_4) nanoparticles. These are not detected in the SXRD in the Mg/Fe system, but could be present as extremely small crystallites or amorphous domains. The emergence of Fe_3C between 600 and 700 °C is correlated to the thermogravimetric analysis (Figure S9) and DTG (Figure S10) plots. A control sample of 100 mol% Fe (MF100) shows a sharp mass loss at 600 °C, representing carbothermal reduction of Fe_3O_4 to Fe_3C with corresponding loss of CO_2. A similar mass loss (shown most clearly by a peak in the DTG) is evident for samples MF25 and MF50, but not for the control of 0 mol% Fe (MF0).

Supporting Figures

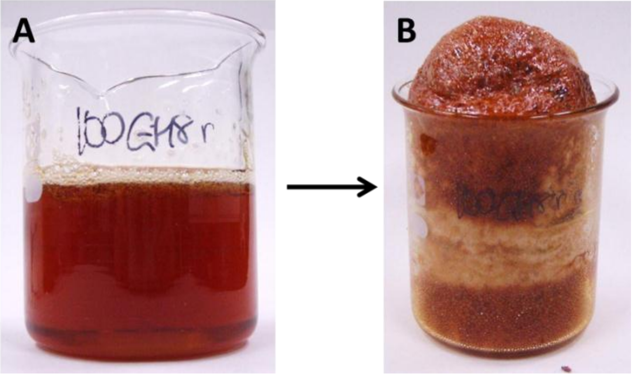

Figure S1 a) Aqueous solution of gelatin, Fe(NO_3)$_3$ and Mg(NO_3)$_2$ and b) expanded sponge-like structure obtained after drying the solution in air at 80 °C.

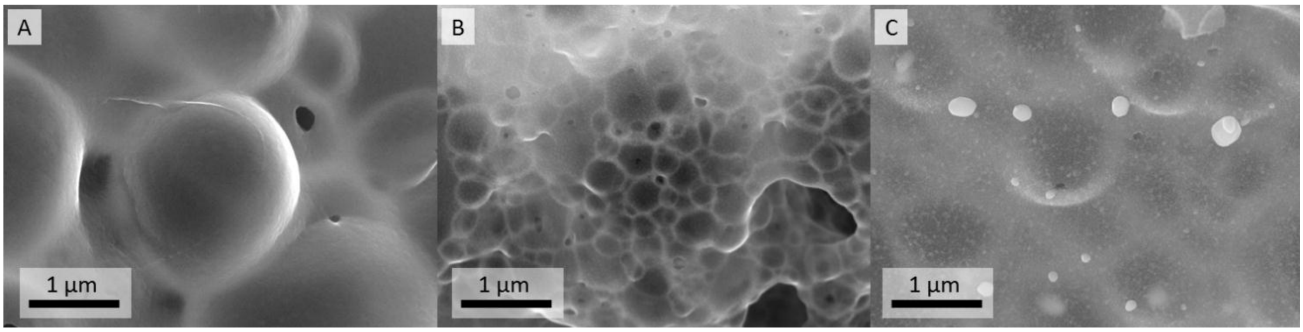

Figure S2 Scanning electron microscope images of sponge samples after calcination under N_2 to 800 °C. Prepared using a total of 0.01 moles of metal salt (nitrates) for 3g of gelatin in all samples and a) 100 mole% Mg, b) 25 mole% Fe, 75 mole% Mg and c) 100 mole% Fe.

Figure S3a Samples prepared by mixing hot gelatin solution with $Mg(NO_3)_2$ solutions of varying concentration then adding a constant amount and concentration of $Fe(NO_3)_3$ solution. From left to right is increasing $[Mg(NO_3)_2]$.

Figure S3b Samples from figure S3a, after boiling the solutions to homogenize.

Figure S3c Samples from figure S3b after drying at 80 °C in air. Left to right is constant [gelatin] and $[Fe(NO_3)_3]$ but increasing $[Mg(NO_3)_2]$.

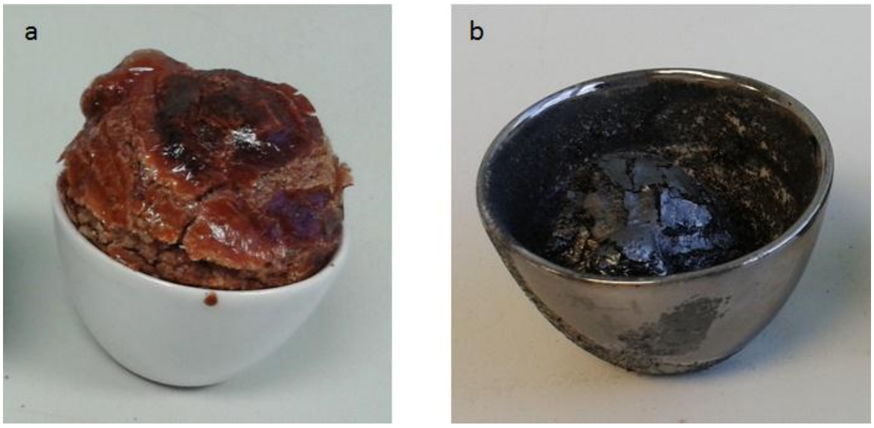

Figure S4 Images of the sponge-like structures a) before and b) after calcination showing the shrinkage of the structure.

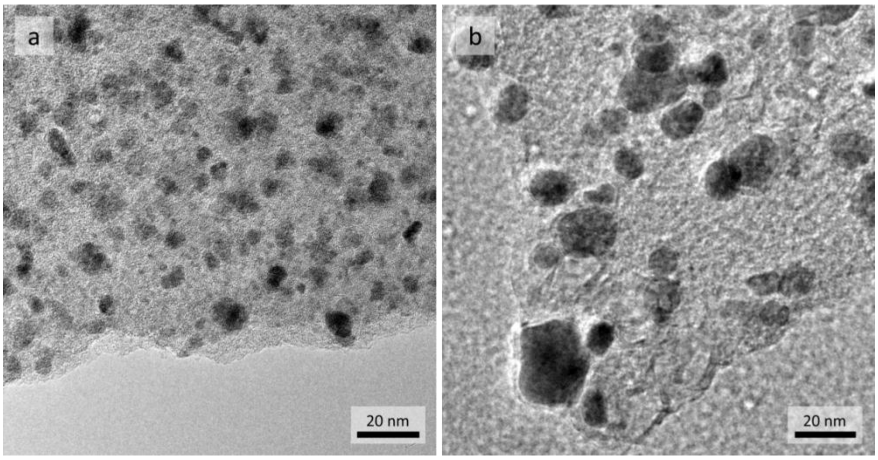

Figure S5 Bright field transmission electron microscope images of Fe_3C/MgO particles embedded in carbon matrix for samples a) MF25 and b) MF50.

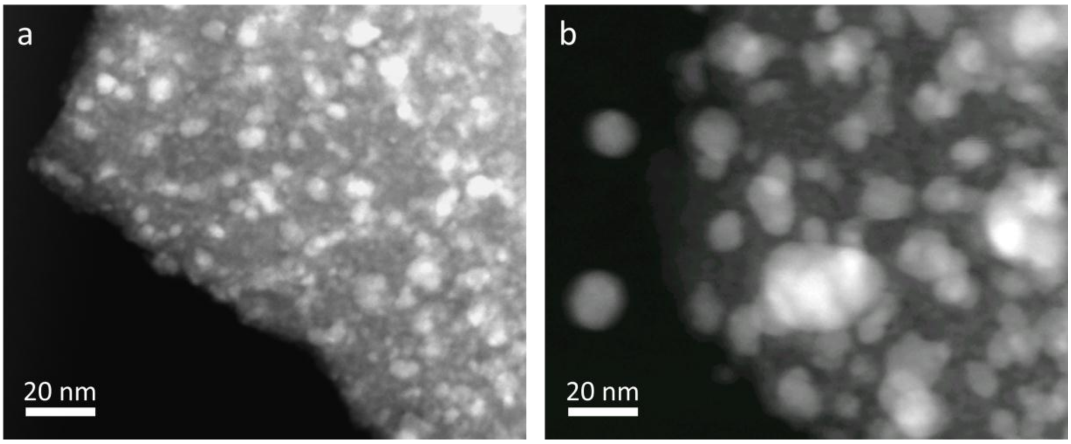

Figure S6 Dark field transmission electron microscope images of Fe_3C/MgO particles embedded in carbon matrix for samples a) MF25 and b) MF50.

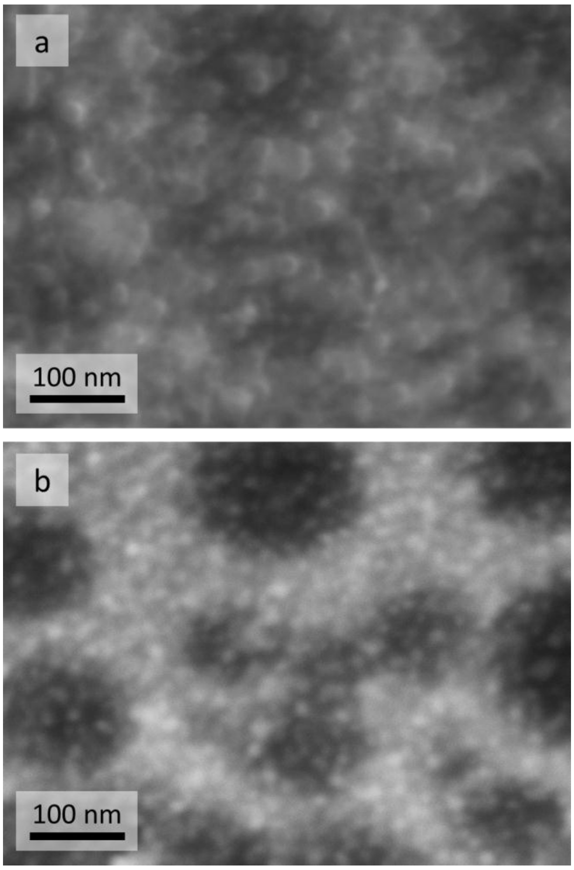

Figure S7 Scanning electron microscope images of an identical sample region using a) SEI and b) COMPO detectors showing the rough surface and spheroidal graphite-coated Fe_3C nanoparticles and the smaller Fe-rich cores (bright spots) respectively.

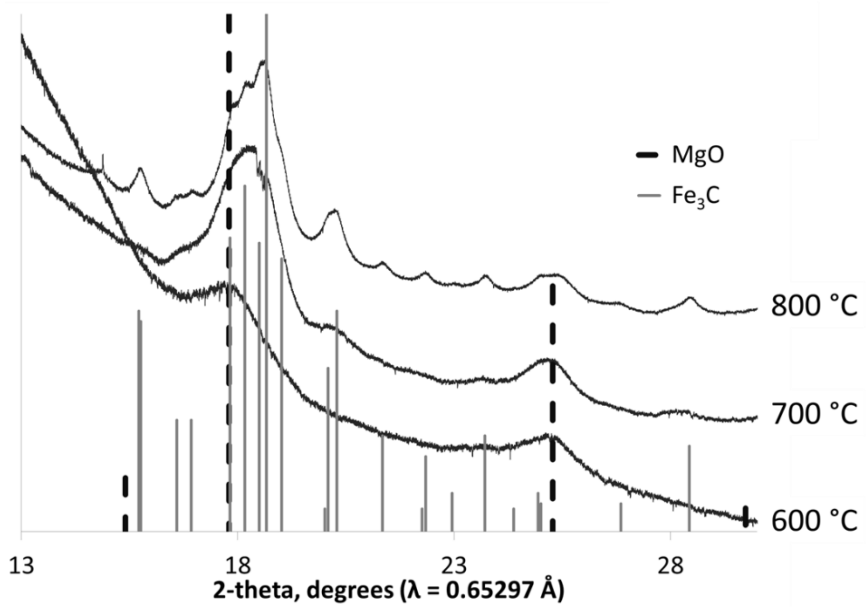

Figure S8 Synchrotron PXRD patterns for samples quenched at 100 °C intervals from 600-800 °C for MF50.

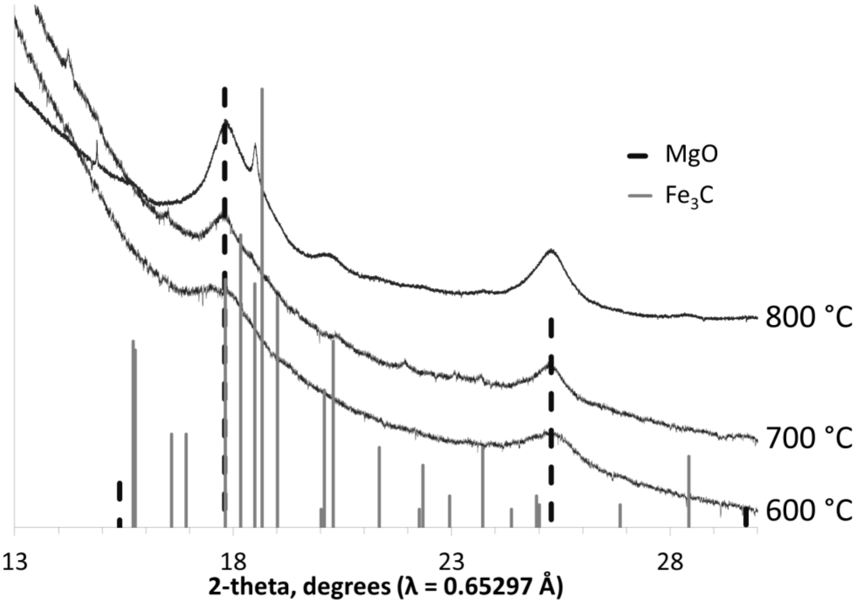

Figure S9 Synchrotron PXRD patterns for samples quenched at 100 °C intervals from 600-800 °C for MF25. Small sharp peaks in the 800 °C sample correspond to metallic Fe.

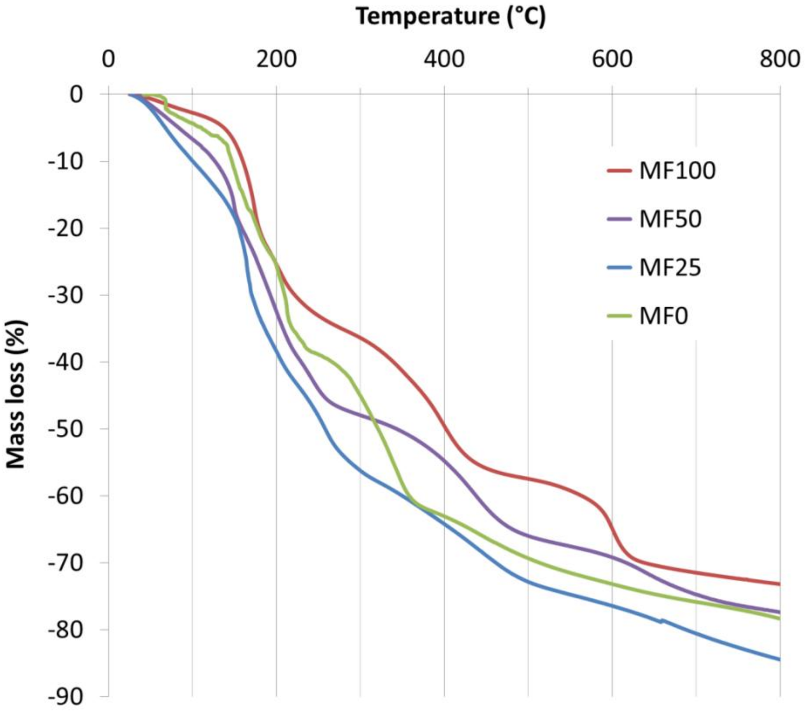

Figure S10 Thermogravimetric analysis under N_2 flow at 10 °C/min of gelatin samples with four different Mg:Fe ratios.

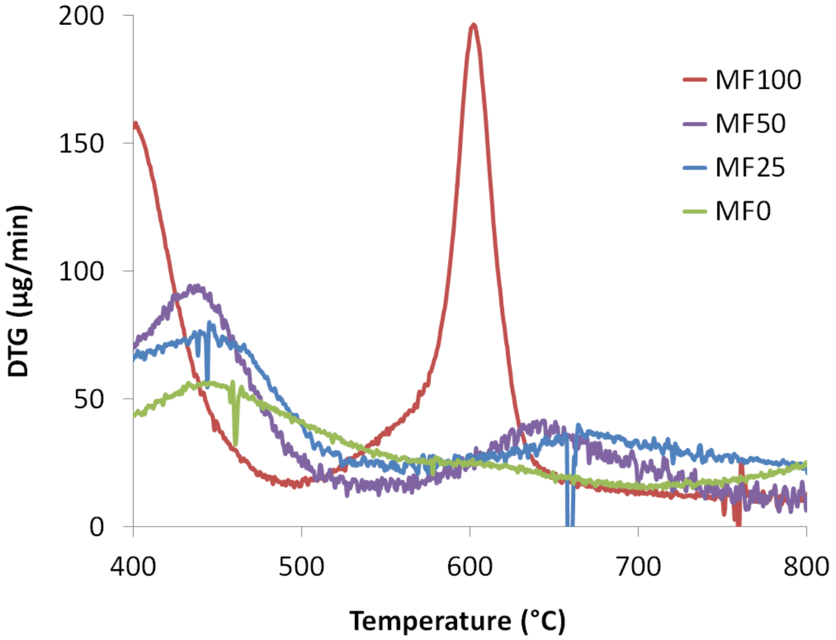

Figure S11 DTG corresponding to TGA data in Figure S8

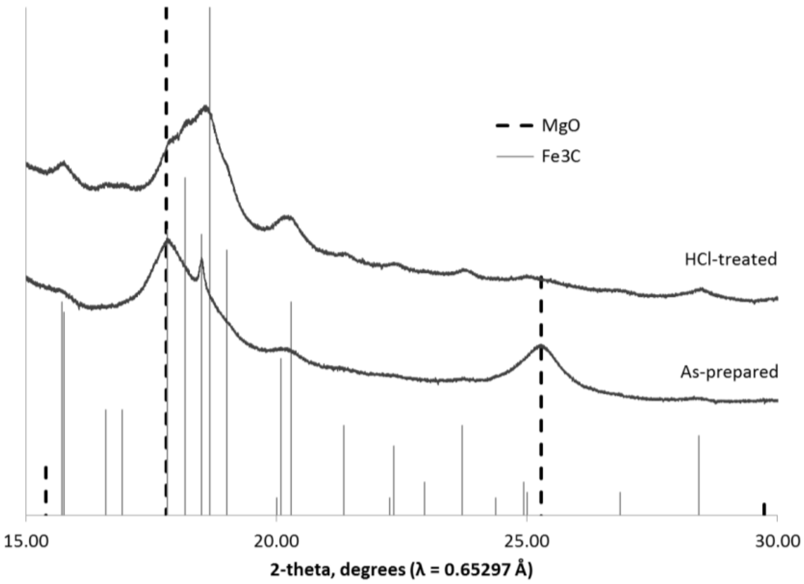

Figure S12 Synchrotron PXRD patterns showing *selective* removal of MgO (no sonication step) from a sample prepared using 25 mol% Fe and 30g of 10% gelatin solution for total 0.01 moles of metals.

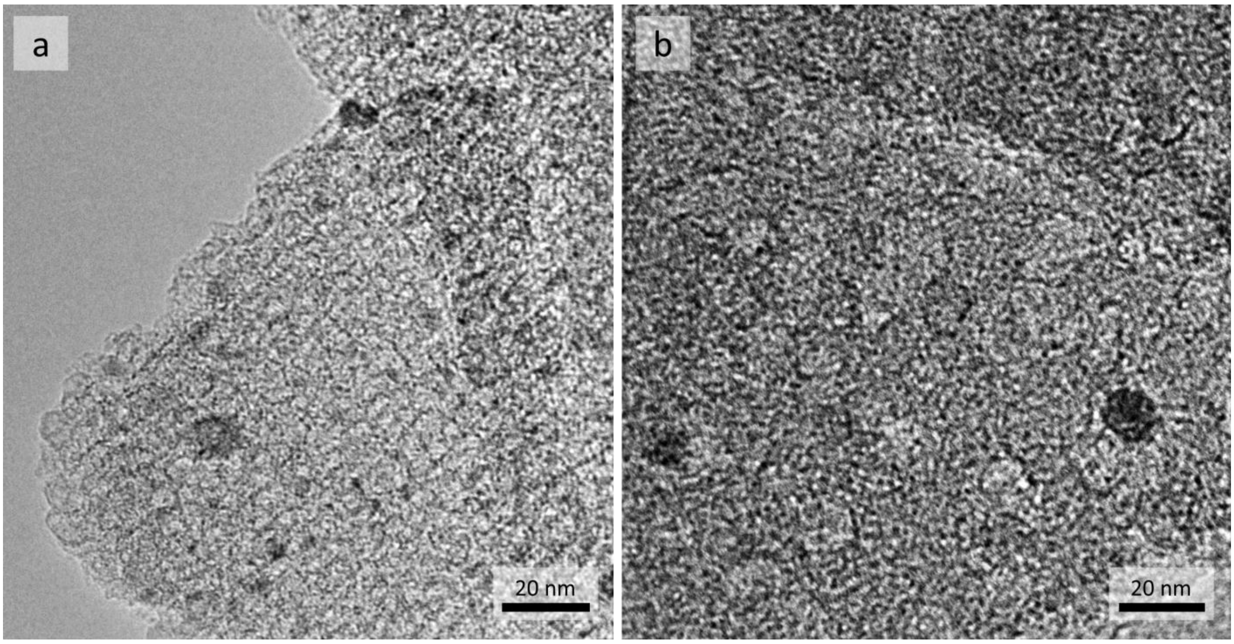

Figure S13 TEM images of a) MF25-E and b) MF50-E showing porous structure.

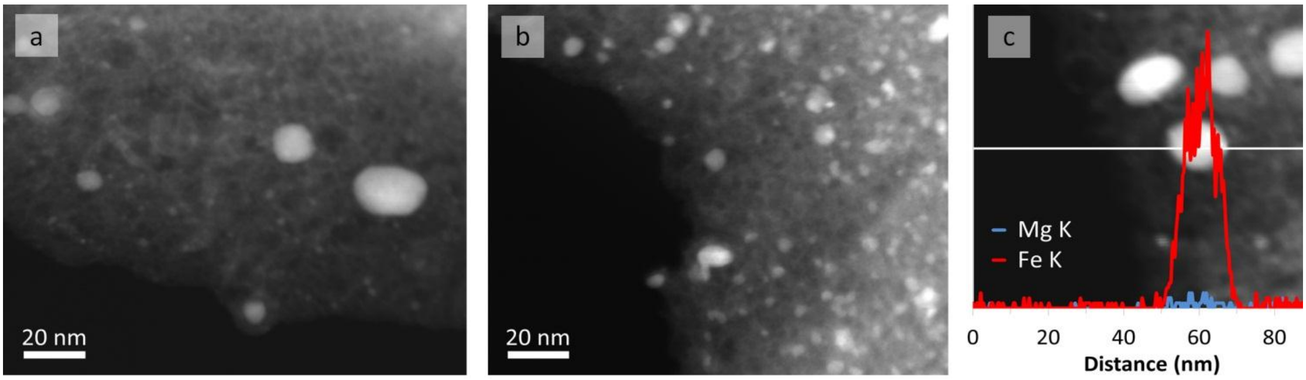

Figure S14 Dark field STEM images of a) MF25-E and b) MF50-E, showing greatly reduced density of bright Fe_3C particles and c) EDXA line scan showing only Fe.

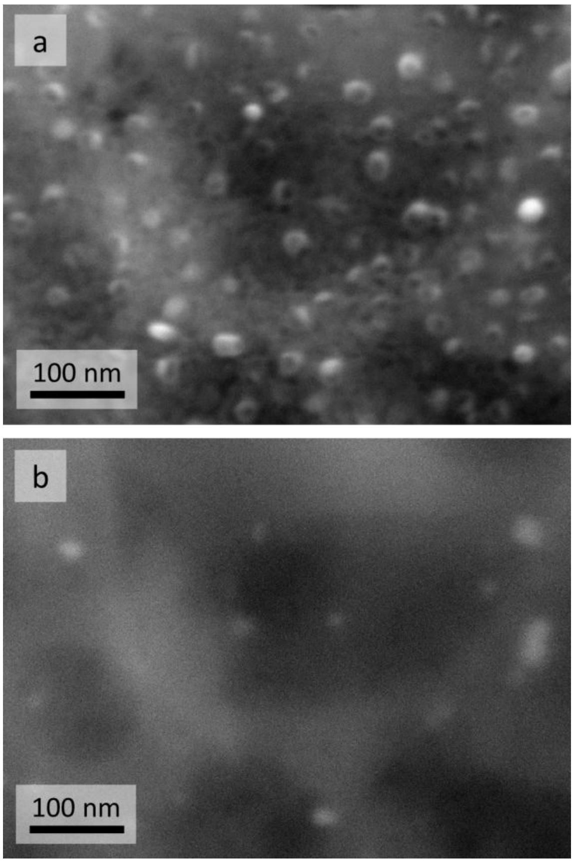

Figure S15 Representative scanning electron microscope images of an identical sample region using a) SEI and b) COMPO detectors showing the porous carbon structure and very few remaining bright spots, indicating removal of most of the iron from the sample (*cf.* Figure S5).

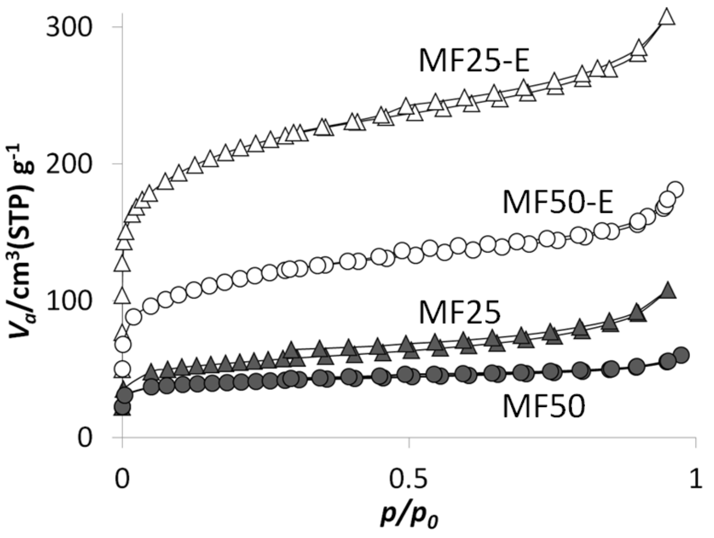

Figure S16 Nitrogen porosimetry data for MF25, MF50, MF25-E and MF50-E

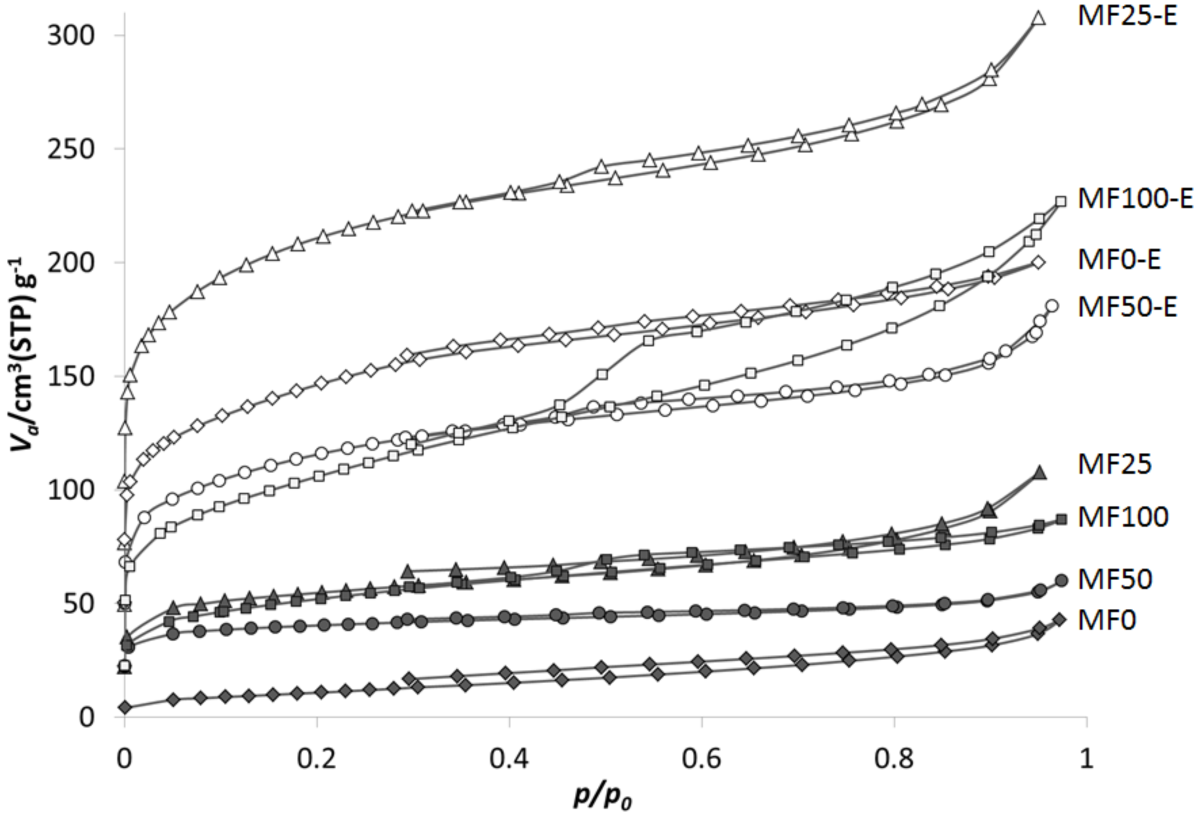

Figure S17 Nitrogen porosimetry data for all samples.

Sample code	**BET surface area (m^2g^{-1})**
MF0	42
MF0HCl	466
MF25	170
MF25HCl	651
MF50	121
MF50HCl	365
MF100	170
MF100HCl	356

Table S2 Full BET data for all samples.

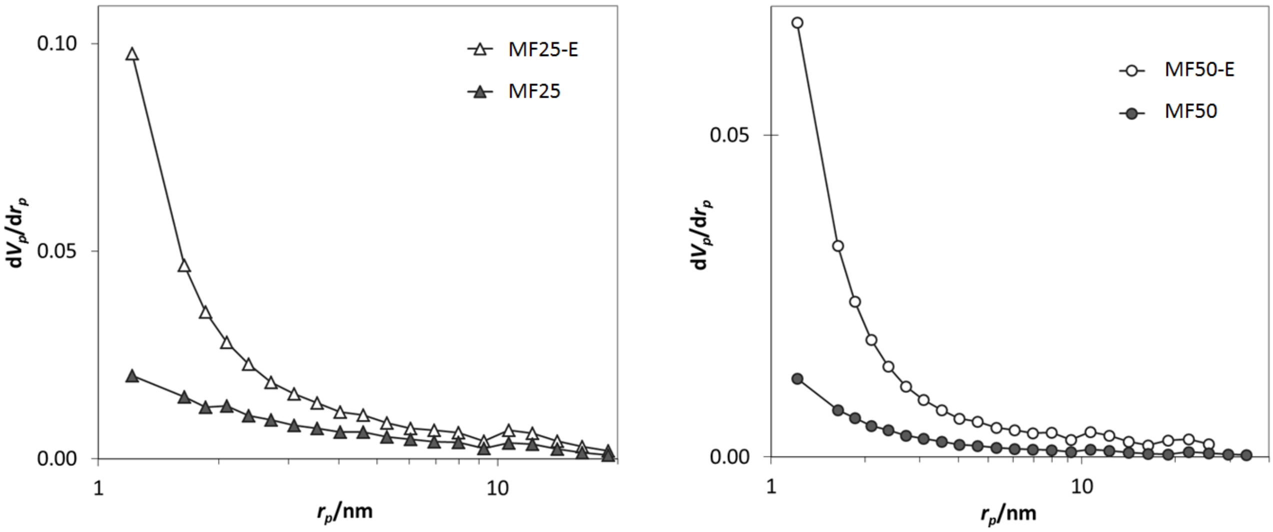

Figure S18 BJH (Barrett-Joyner-Halenda) plots for MF25, MF25-E, MF50 and MF50-E.

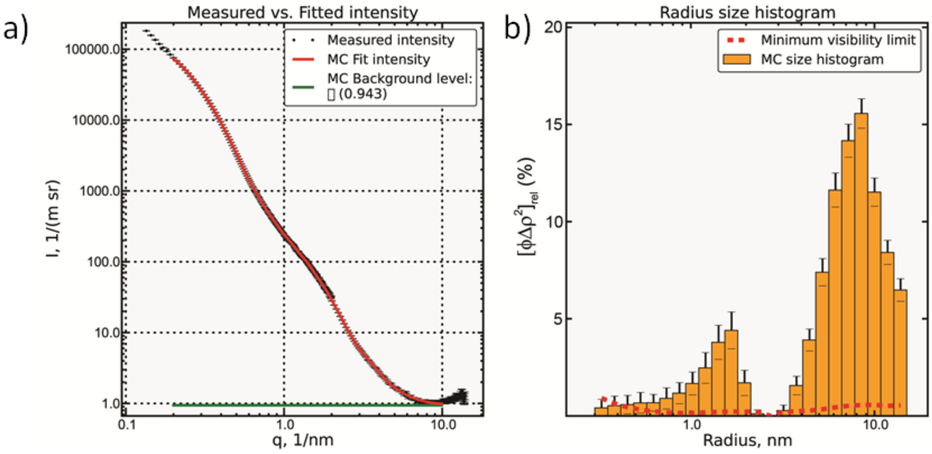

Figure S19 a) Measured small angle X-ray scattering (SAXS) data and fit and b) histogram of calculated radius size distributions for sample MF50, prepared using 50 mol% Fe.

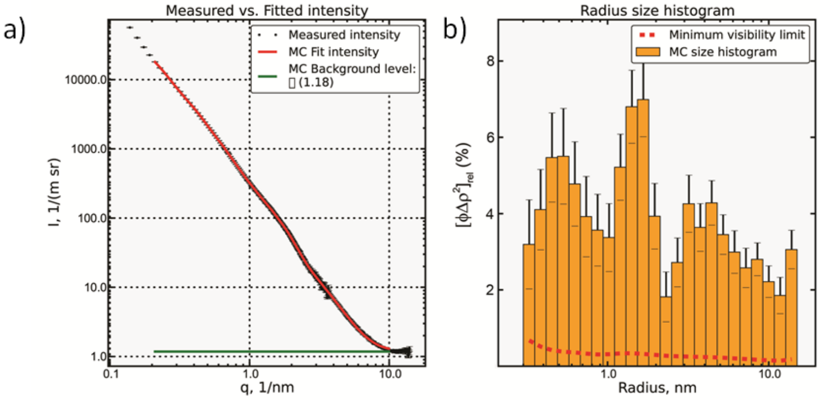

Figure S20 a) Measured small angle X-ray scattering (SAXS) data and fit and b) histogram of calculated radius size distributions for sample MF50-E, prepared using 50 mol% Fe and etched with 0.1 M HCl.

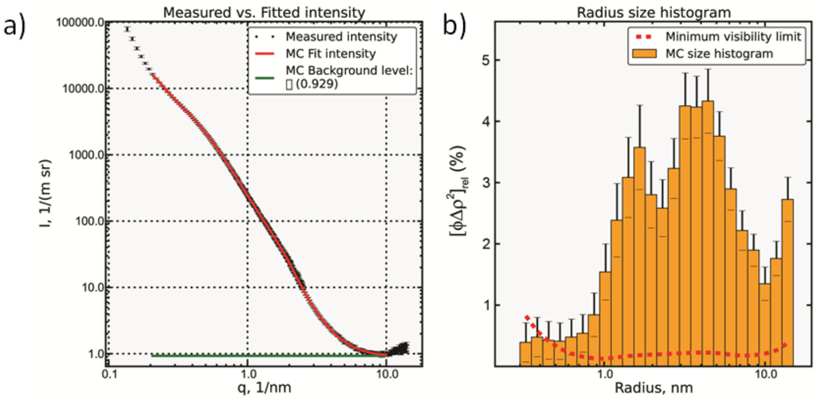

Figure S21 a) Measured small angle X-ray scattering (SAXS) data and fit and b) histogram of calculated radius size distributions for sample MF25, prepared using 25 mol% Fe.

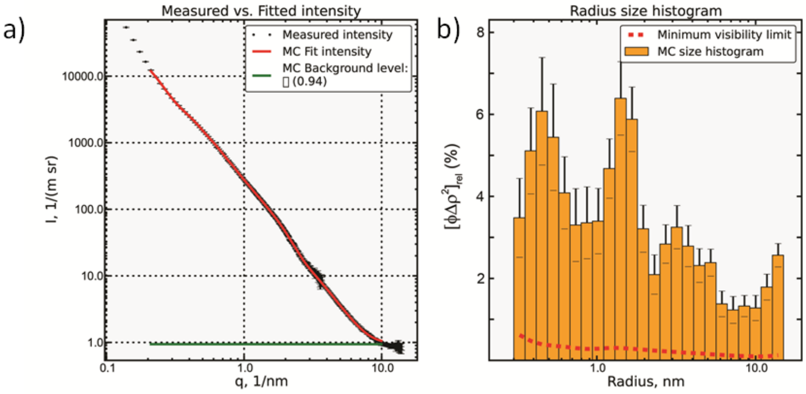

Figure S22 a) Measured small angle X-ray scattering (SAXS) data and fit and b) histogram of calculated radius size distributions for sample MF50-E, prepared using 50 mol% Fe and etched with 0.1 M HCl.

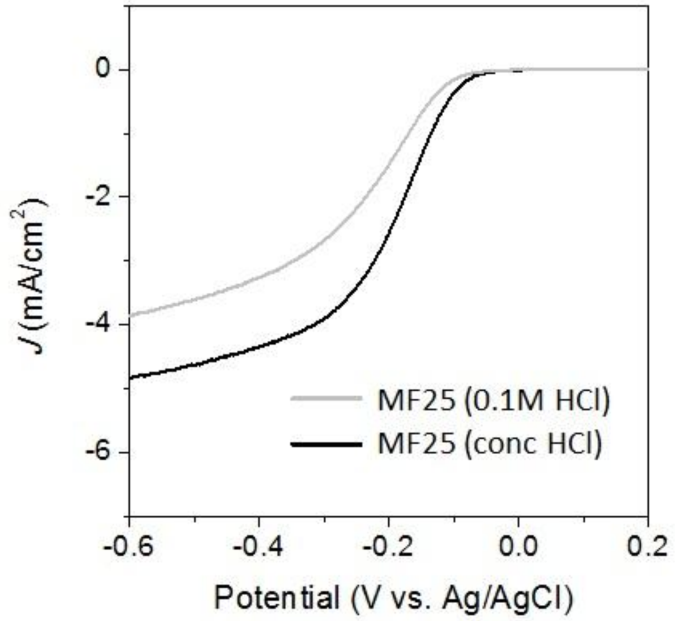

Figure S23 Rotating-disk voltammograms of sample MF25 treated with 0.1M and conc HCl, at a rotation rate of 2500 rpm in an O_2-saturated 0.1 M KOH aqueous solution at a scan rate of 10 mV/s.

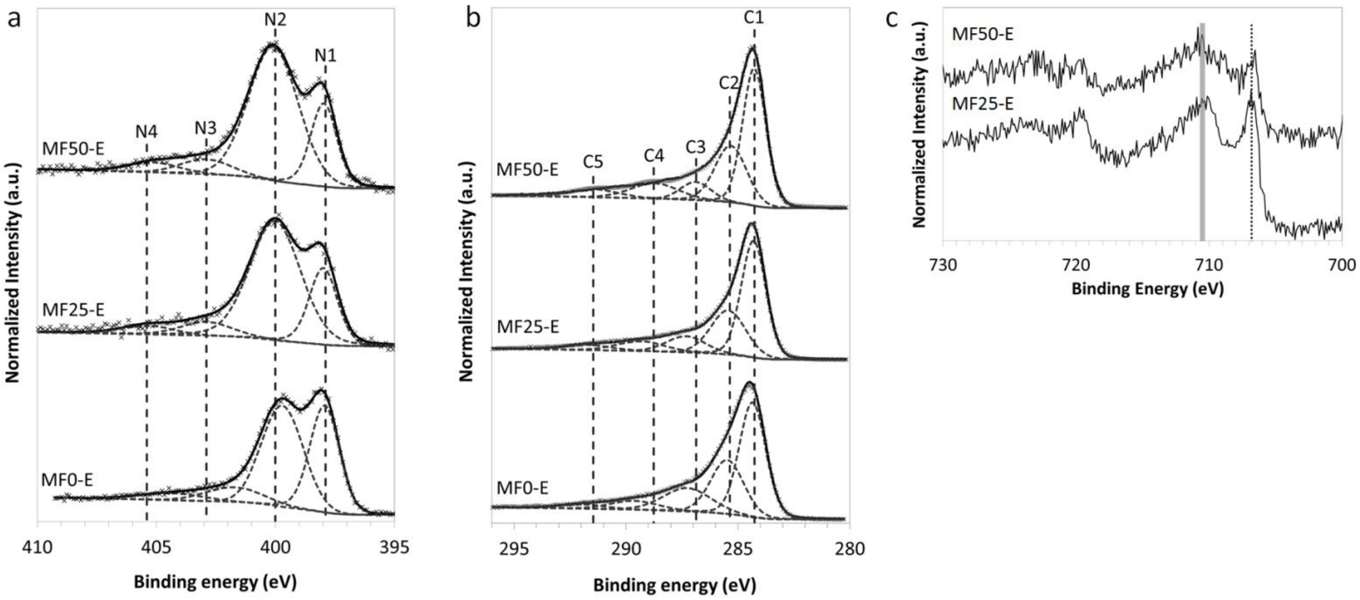

Figure S24 XPS spectra for a) nitrogen 1s b) carbon 1s peaks and c) iron 2p peaks for acid-etched samples. All the binding energies are referenced to C1s at 284.3 eV.

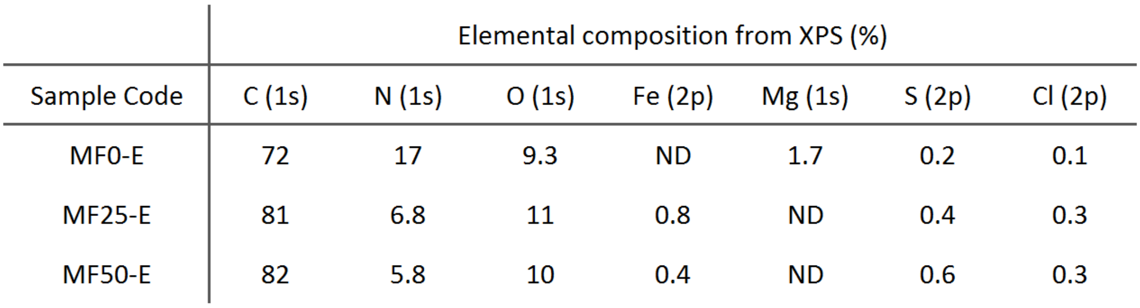

	Elemental composition from XPS (%)						
Sample Code	C (1s)	N (1s)	O (1s)	Fe (2p)	Mg (1s)	S (2p)	Cl (2p)
MF0-E	72	17	9.3	ND	1.7	0.2	0.1
MF25-E	81	6.8	11	0.8	ND	0.4	0.3
MF50-E	82	5.8	10	0.4	ND	0.6	0.3

Table S3 Full elemental composition from XPS. NB: the higher nitrogen content in MF0-E suggests that some nitrogen is lost from the system on graphitization. This is consistent with previous reports of iron-catalyzed graphitization.[8]

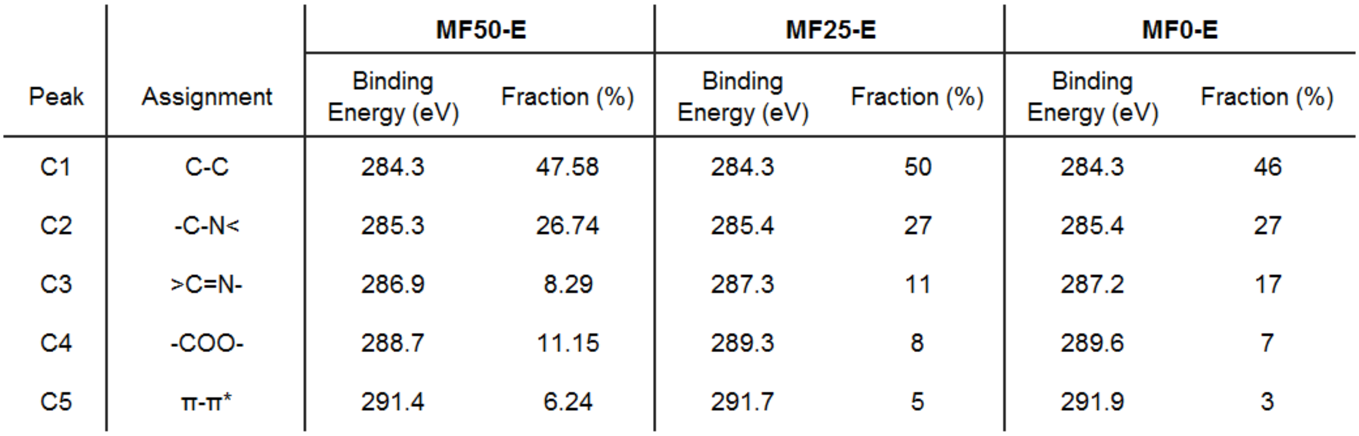

Peak	Assignment	MF50-E		MF25-E		MF0-E	
		Binding Energy (eV)	Fraction (%)	Binding Energy (eV)	Fraction (%)	Binding Energy (eV)	Fraction (%)
C1	C-C	284.3	47.58	284.3	50	284.3	46
C2	-C-N<	285.3	26.74	285.4	27	285.4	27
C3	>C=N-	286.9	8.29	287.3	11	287.2	17
C4	-COO-	288.7	11.15	289.3	8	289.6	7
C5	π-π*	291.4	6.24	291.7	5	291.9	3

Table S4 Percentage areas of deconvoluted carbon 1s peaks from XPS

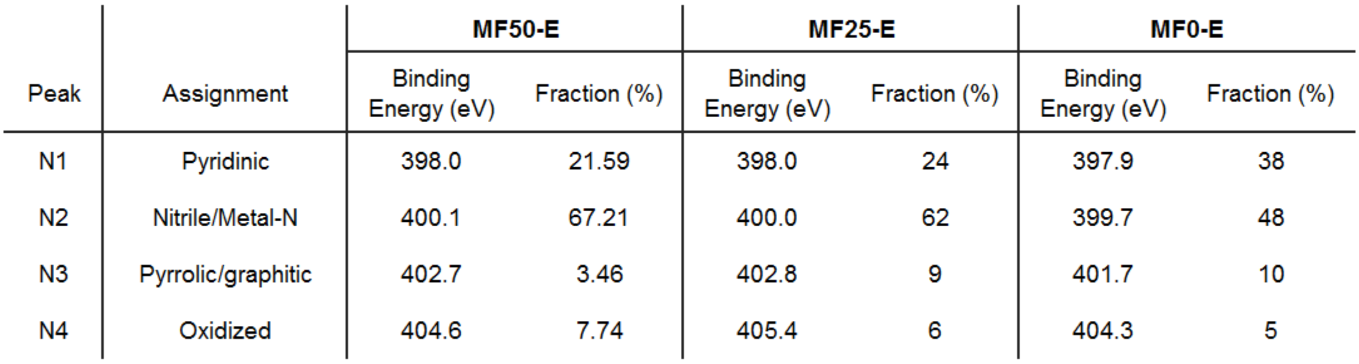

Peak	Assignment	MF50-E		MF25-E		MF0-E	
		Binding Energy (eV)	Fraction (%)	Binding Energy (eV)	Fraction (%)	Binding Energy (eV)	Fraction (%)
N1	Pyridinic	398.0	21.59	398.0	24	397.9	38
N2	Nitrile/Metal-N	400.1	67.21	400.0	62	399.7	48
N3	Pyrrolic/graphitic	402.7	3.46	402.8	9	401.7	10
N4	Oxidized	404.6	7.74	405.4	6	404.3	5

Table S5 Percentage areas of deconvoluted nitrogen 1s peaks from XPS

NB: The small sulfur peak in XPS of all samples can be attributed to sulfur-containing amino acid residues such as methionine in the parent gelatin and the trace of chlorine probably derives from the HCl washing step.

Supporting References

---

[1] M. Tanaka, T. Katsuya, A. Yamamoto, *Rev. Sci. Instrum.* **2008**, *79***,** 075106.

[2] B. R. Pauw, J.-S. Pedersen, S. Tardif, M. Takata, B. B. Iversen, arXiv:1210.5304 **2012**, http://arxiv.org/abs/1210.5304; *J. Appl. Cryst.* **2013**, doi:10.1107/S0021889813001295.

[3] F. Zhang, J. Ilavsky, G. G. Long, J. P. G. Quintana, A. J. Allen, P. R. Jemain, *Metall. Mater. Trans. A* **2010**, *41A*, 1151-1158.

[4] B. R. Pauw, J.-S. Pedersen, S. Tardif, M. Takata, B. B. Iversen, arXiv:1210.5304 (2012).at <http://arxiv.org/abs/1210.5304>

[5] N. Hu, N. Borkar, D. Kohls, D. W. Schaefer, *J. Membrane Sci.* **2011**, *379*, 138–145.

[6] Z. Mileeva *et al*. *Carbon*, **2012**, *50*, 5062–5075.

[7] Z. Schnepp, S. C. Wimbush, C. Giordano, M. Antonietti, *Chem. Mater.* **2010**, *22*, 5340-5344.

[8] Y. Ohtsuka, Z. Wu, *Energy Fuels*, **2009**, *23*, 4774–4781.